Thermomechanical Contact Analysis of Semi-infinite Solids With Fractal Surface Topographies

Z.-Q. Gong, Graduate Student
K. Komvopoulos, Professor, Fellow ASME

Department of Mechanical Engineering
University of California
Berkeley, CA 94720

Abstract

A thermomechanical analysis is presented for an elastic semi-infinite solid in contact with a rigid rough surface characterized by fractal geometry. A piecewise-linear distribution of the contact pressure was obtained by the superposition of overlapping triangular pressure elements. The normal surface displacements caused by the contact pressure, shear traction, and thermoelastic distortion due to frictional heating are incorporated in the influence coefficients used in the matrix inversion method. Results for a smooth cylindrical surface sliding over a semi-infinite elastic medium demonstrate the accuracy of the analysis and provide a reference for comparison with the results obtained with the rough (fractal) surface. The effects of the surface topography and the interaction between neighboring asperity microcontacts on the surface and subsurface temperature rise and stress field of the elastic semi-infinite medium are discussed in the context of analytical results. The significance of frictional heating on the contact pressure, temperature rise, and stresses is interpreted in terms of the Peclet number and topography (fractal) parameters. The results provide insight into the likelihood for cracking and plastic flow at the surface due to the combined effects of mechanical and thermal surface loads.

Submitted to the ASME *Journal of Tribology* on January 14, 2004.

1. Introduction

Frictional heating and the resulting temperature rise may significantly affect the mechanical response of interacting surfaces. Knowledge of the thermoelastic stresses in sliding solid bodies with rough surfaces is essential in failure analysis of mechanical systems. The determination of the thermal and thermoelastic fields in semi-infinite homogeneous media due to different surface heat sources has been the objective of several past studies. One of the pioneering analyses is attributed to Blok (1937) who examined the flash temperature and maximum surface temperature rise in a semi-infinite elastic body subjected to a uniform square heat source moving at high and low Peclet numbers. Jaeger (1942) extended the previous analysis to the intermediate regime of Peclet number. These early studies established the foundation of subsequent thermomechanical studies, both analytical and numerical.

Based on a Green's function method, Tian and Kennedy (1994) determined the surface temperature rise in a semi-infinite body due to different moving heat sources. Ju and Huang (1982) performed a thermomechanical analysis of homogeneous half-spaces subjected to a fast moving heat source and showed predominantly compressive stresses at the surface. Ju and Huang (1982) and Ju and Liu (1988) observed that the maximum thermal tensile stress occurs slightly below the trailing edge of the contact region at a depth controlled by the Peclet number. Leroy et al. (1989) conducted a two-dimensional analysis of a layered medium subjected to a translating heat source and reported high stresses in the surface layer when its thermomechanical properties differed significantly from those of the substrate. Ju and Farris (1997) obtained thermal and thermoelastic solutions in the frequency domain for an arbitrary heat source moving over an elastic half-space. Liu and Wang (2003) investigated the transient thermoelastic stress

fields generated in a half-space due to either a parabolic or irregularly distributed heat source moving at constant velocity.

In the previous studies, the *a priori* assumed distribution of the heat sources was assumed to be unaffected by the mechanical response of the deformed medium. To consider the effect of frictional heating on contact deformation, it is necessary to account for the coupling of mechanical and thermal stresses. In view of the complex fully coupled thermomechanical contact problems, the majority of the earlier analyses have been based on the finite element method. Gupta et al. (1993) used a two-dimensional finite element model to study rolling and sliding over a semi-infinite medium under the assumption of invariant contact pressure. Cho and Komvopoulos (1997) investigated subsurface crack propagation using the finite element technique. Ye and Komvopoulos (2003) developed a finite element model to examine the simultaneous effects of mechanical and thermal surface traction on the deformation of elastic-plastic layered media. Gong and Komvopoulos (2004) conducted a fully coupled finite element analysis of an elastic-plastic layered medium with a patterned surface in contact with an elastic-plastic sphere. Wang and Liu (1999, 2000) introduced a two-dimensional thermoelastic contact model of two infinitely large rough surfaces that accounts for the thermal effect on the mechanical response, and Liu and Wang (2001) extended the previous analysis to a three-dimensional thermomechanical model of non-conforming contacts.

Although the previous studies have provided useful insight into the temperature and thermoelastic stress fields in solids subjected to either moving heat sources or sliding rough surfaces, analytical thermomechanical analysis for rough surfaces elucidating the dependence of the temperature and stress fields on the surface topography and Peclet number has not been reported yet. Therefore, the objective of this study was to develop a thermomechanical contact

model for semi-infinite media possessing fractal surface topographies that accounts for the simultaneous effects of thermal and mechanical deformations. Results are presented for the contact pressure distribution and surface and subsurface temperature and stress fields in terms of Peclet number and surface topography (fractal) parameters. The significance of mechanical surface traction and frictional heating on the propensity for yielding and cracking at the sliding surface are interpreted in light of numerical results.

2. Surface Characterization

Surface topography parameters based on traditional statistical theories depend on the sample length and instrument resolution. To overcome these limitations, the surface topography can be characterized by fractal geometry (Mandelbrot, 1983). The surface topography can be represented by the Weierstrass-Mandelbrot (W-M) function (Berry and Lewis, 1980), which exhibits continuity, non-differentiability, and self-affinity over a range of scale lengths, given by (Wang and Komvopoulos, 1994)

$$z(x) = L\left(\frac{G}{L}\right)^{(D-1)} \sum_{n=0}^{n_{\max}} \frac{\cos(2\pi\gamma^n x / L)}{\gamma^{(2-D)n}}, \tag{1}$$

where L is the fractal sample length in the x direction, G is the fractal roughness parameter that is independent of frequency, D ($1 < D < 2$) is the fractal dimension that determines the contribution of high and low frequency components in the surface function (i.e., high values of D correspond to smooth surfaces), g ($\gamma > 1$) is a scaling parameter (typically, $g = 1.5$ (Komvopoulos and Yan, 1997)), and n is a frequency index with $n_{\max} = \text{int}[\log(L/L_s)/\log\gamma]$ representing the upper limit of n, where int[…] denotes the integer part of the number in the bracket and L_s is the cut-off length. The scale-independent fractal parameters G and D can be determined experimentally

from a log-log plot of the structure function of the surface profile $z(x)$ versus wavelength (Komvopoulos, 2000).

3. Thermomechanical Contact Analysis

Sliding friction leads to energy dissipation in the form of heat within the vicinity of the real contact area. The frictional heat dissipated is responsible for the temperature rise resulting in the development of thermal stresses and variations in the real contact area and contact pressure distribution due to thermal expansion. Because such changes affect heat generation rate and heat conduction across the contact interface, the thermal and mechanical stress and strain fields are fully coupled. Therefore, the determination of the thermal and mechanical fields must be determined simultaneously.

3.1 Surface Deformation and Temperature Field

Thermomechanical contact of two rough surfaces can be studied using the equivalent model of a rigid and adiabatic surface with roughness equivalent to the effective roughness of the two original surfaces in contact with a deformable semi-infinite medium possessing a smooth surface and effective material properties, as shown schematically in Fig. 1. Coulomb friction is assumed at the contact interface. The elastic medium is subjected to normal and tangential (friction) surface tractions, yielding a total normal load, P, in the z direction and a total tangential load, $F = mP$, in the x direction, where m is the coefficient of friction. Frictional heat at each asperity microcontact is conducted into the elastic medium. Similar to the treatment of Carslaw and Jaeger (1959), coordinate system (x, y, z) fixed with the moving rough surface and system (x', y', z') fixed with the stationary elastic medium are used in the analysis. The two coordinate systems are related by

$$x = x' - Vt \qquad z = z', \tag{2}$$

where t is the time. The heat flux density due to frictional heat, q, is given by

$$q = h\mu pV, \tag{3}$$

where h is the fraction of mechanical work dissipated as heat, and p is the contact pressure. It is assumed that h = 1.0, i.e., nearly all the energy dissipated in a frictional contact is converted to heat, consistent with the conclusion of Uetz and Föhl (1978). Because the rough surface is modeled to be adiabatic, the generated frictional heat, q, is entirely conducted into the elastic medium.

The normal displacement in sliding contact is due to the effects of contact pressure, shear traction, and thermoelastic distortion induced by frictional heating. Hence, the normal displacement at the surface, u_z, can be expressed as,

$$u_z = u_z^N + u_z^S + u_z^T, \tag{4}$$

where u_z^N, u_z^S, and u_z^T are the normal displacements due to the contact pressure, shear traction, and frictional heating, respectively. Each microcontact area is divided into a number of small segments of equal width, b. A piecewise-linear distribution of the contact pressure is obtained by superposition of overlapping triangular pressure elements (Johnson, 1985).

The normal surface displacement due to the triangular pressure distribution shown in Fig. 2(a) is given by (Johnson, 1985)

$$u_z^N = -\frac{(1-\nu^2)}{2\pi E}\frac{p_0}{b}\left\{(x+b)^2 \ln\left(\frac{x+b}{b}\right)^2 + (x-b)^2 \ln\left(\frac{x-b}{b}\right)^2 - 2x^2 \ln\left(\frac{x}{b}\right)^2\right\} + C, \tag{5}$$

where p_0 is the maximum contact pressure, E and ν are the elastic modulus and Poisson ratio of the semi-infinite solid, and C is a constant determined by choosing a point on the z axis at a distance d below the surface as a reference for the normal displacements. The surface

displacement in the z direction due to the triangular shear traction distribution shown in Fig. 2(a) is obtained as (Johnson, 1985)

$$u_z^S = \begin{cases} \dfrac{(1-2n)(1+n)}{E}\dfrac{q_0}{b}x(b-\dfrac{1}{2}|x|) & |x| \le b \\ \dfrac{(1-2n)(1+n)}{E}\dfrac{q_0 b}{2} & x > b \\ -\dfrac{(1-2n)(1+n)}{E}\dfrac{q_0 b}{2} & x < -b \end{cases} \tag{6}$$

where q_0 is the peak value of the shear traction. A triangular distribution of a heat source moving from left to right at velocity V is shown in Fig. 2(b). For convenience, the following non-dimensional parameters are introduced in the analysis,

$$\xi = \frac{x}{b}, \quad \zeta = \frac{z}{b}, \quad \eta = \frac{x'}{b}. \tag{7}$$

The thermoelastic distortion at the surface due to a moving heat source of triangular distribution can be obtained by superposition of the moving line heat source solutions (Barber, 1984), which can be expressed as

$$u_z^T = \begin{cases} l & x \le -1 \\ l\int_{-1}^{1}(1-|h|)e^{-Pe(x-h)}I_0[Pe(x-h)]dh & x \ge 1 \\ l\left\{\int_{-1}^{x}(1-|h|)e^{-Pe(x-h)}I_0[Pe(x-h)]dh + \dfrac{1}{2} - x + \dfrac{1}{2}x^2\,\mathrm{sgn}(x)\right\} & -1 \le x \le 1 \end{cases} \tag{8}$$

where I_0 is the modified zero-order Bessel function of the first kind, sgn(x) is a sign function of x, and l is defined as

$$l = -\frac{aq_0^T(1+n)b^2}{rckPe}, \tag{9}$$

where q_0^T is the peak value of the heat flux, Pe is the Peclet number, defined as $Vb/2k$, and a, r, c, and k are the thermal expansion, mass density, specific heat, and thermal diffusivity of the semi-infinite solid medium, respectively.

Therefore, the total surface displacement in the z direction can be obtained by summing the displacement components given by Eqs. (5), (6), and (8) at each microcontact and then integrating over all the asperity microcontacts comprising the real contact area,

$$u_z(x) = \sum_{i=1}^{N} \sum_{j=1}^{M_i - 1} [u_z^N \Big|_i^j (x) + u_z^S \Big|_i^j (x) + u_z^T \Big|_i^j (x)], \tag{10}$$

where N is the total number of asperity microcontacts, M_i is the total number of segments in the ith asperity microcontact, and $u_z^N \Big|_i^j$, $u_z^S \Big|_i^j$, and $u_z^T \Big|_i^j$ are the normal surface displacements at the ith asperity microcontact due to the triangular distributions of contact pressure, shear traction, and frictional heat, respectively, at the jth asperity microcontact.

Since q_0^T and q_0 can be expressed as functions of p_0, i.e.,

$$q_0^T = h m p_0 V, \qquad q_0 = m p_0, \tag{11}$$

it follows that Eq. (10) represents a set of $\sum_{i=1}^{N} M_i$ simultaneous equations that can be expressed in matrix form,

$$\{U_Z\} = \{C\}\{P\}, \tag{12}$$

where $\{U_Z\}$ is the matrix of the normal surface displacements, $\{P\}$ is the contact pressure matrix, and $\{C\}$ is square and symmetric matrix termed the influence coefficient matrix. A procedure based on the matrix inversion method, which is similar to that used by Bailey and Sayles (1991) to determine the subsurface stresses in rough surfaces subjected to both normal and tangential forces, was used to solve Eq. (12). Since both the contact pressure and the real

contact area are unknown, the following iteration procedure was used to solve Eq. (12). First, the initial surface displacement matrix $\{U_z\}$ was determined by truncating the rough surface by a plane to a maximum surface interference, $d_{\max}$, and the corresponding contact pressure was calculated from $\{P\} = \{C^{-1}\}\{U_z\}$. Any triangular pressure elements exhibiting negative pressure violate the requirement $p > 0$ and were removed from the assumed contact region. Then, the surface displacement was recalculated using Eq. (12) and any overlapping points were added to the assumed contact region. With the new set of contact points, Eq. (12) was solved again to obtain the contact pressure $\{P\}$. This iteration procedure was repeated until conditions of (a) positive contact pressure, (b) no surface penetration, and (c) contact only within the current contact region were satisfied.

Following an approach similar to that for a uniform band heat source (Carslaw and Jaeger, 1959), the temperature rise due to a heat source of triangular distribution is found to be

$$\Delta T = \frac{q_0^T b}{pk} \int_{-1}^{1} (1-|h|) e^{-Pe(x+h)} K_0\{Pe[(x+h)^2 + z^2]^{1/2}\} dh \,, \tag{13}$$

where k is the thermal conductivity of the semi-infinite solid, and K_0 is the modified zero-order Bessel function of the second kind. Therefore, the temperature rise at a point (x, z), obtained by superimposition, is given by

$$\Delta T(x,z) = \sum_{i=1}^{N} \sum_{j=1}^{M_i - 1} \Delta T\Big|_i^j (x,z) \,, \tag{14}$$

where $\Delta T\Big|_i^j (x,z)$ is the temperature rise at the ith asperity microcontact due to the jth triangular distribution of heat flux.

3.2 Stress Field

The stress field in the elastic semi-infinite medium due to contact with the rough surface can be obtained by superposition of the stress fields generated by the triangular distributions of contact pressure, shear traction, and heat flux at each microcontact. The stresses in the elastic solid due to a moving heat source with the triangular distribution shown in Fig. 2(b) were obtained in the frequency domain using spatial Fourier transformation, following an analytical approach similar to that of Ju and Farris (1997),

$$\hat{s}_{xx}^{T} = \frac{Ea\hat{T}_0}{(1-n)b}\{[2(b_2 + b_1 i)\,\mathrm{sgn}(w) - wi - wz(b_2 + b_1 i - |w|i)]e^{-|w|z} - (b + wi)e^{(b_2 i - b_1)z}\} \tag{15}$$

$$\hat{s}_{zz}^{T} = \frac{Ea\hat{T}_0}{(1-n)b}\{[-wi + wz(b_2 + b_1 i - |w|i)]e^{-|w|z} + wie^{(b_2 i - b_1)z}\} \tag{16}$$

$$\hat{s}_{xz}^{T} = \frac{Ea\hat{T}_0}{(1-n)b}\{[b_2 i - b_1 - |w|z(b_2 i - b_1 + |w|)]e^{-|w|z} + (b_1 - ai)e^{(b_2 i - b_1)z}\} \tag{17}$$

where $i = \sqrt{-1}$, and parameters b, b_1, b_2, and $\hat{T}_0$ are defined as

$$b = V / k \tag{18}$$

$$b_1 = \sqrt{\frac{w^2 + \sqrt{w^4 + w^2 b^2}}{2}} \tag{19}$$

$$b_2 = \frac{bw}{2b_1} \tag{20}$$

$$\hat{T}_0 = \frac{2[1-\cos(b_2 w)]}{b_2 w^2 k(b_1 - b_2 i)}. \tag{21}$$

The spatial stress field due to frictional heating can be obtained by applying inverse Fourier transformation to the numerical solution derived in the frequency domain, i.e.,

$$s^{T}(x,z) = \int_{-\infty}^{+\infty} \hat{s}^{T}(w,z)e^{iwx}\,dw, \tag{22}$$

where s^{T} and $\hat{s}^{T}$ denote thermal stress components in the spatial and frequency domains, respectively. The numerical thermoelastic stresses for a moving line heat source obtained with this method were found to be in good agreement with the analytical results of Barber (1984). Closed-form solutions for the stresses due to normal and shear tractions possessing triangular distributions have been obtained by Johnson (1985). Consequently, the stress at any point *A(x, z)* in the solid can be expressed as

$$s(x,z) = \sum_{i=1}^{N} \sum_{j=1}^{M_i - 1} [s^{N}\Big|_{i}^{j}(x,z) + s^{S}\Big|_{i}^{j}(x,z) + s^{T}\Big|_{i}^{j}(x,z)], \tag{23}$$

where $s^{N}\Big|_{i}^{j}$, $\sigma^{S}\Big|_{i}^{j}$, and $s^{T}\Big|_{i}^{j}$ are the stresses at the *i*th asperity microcontact due to the *j*th triangular distributions of contact pressure, shear traction, and heat flux, respectively.

4. Results and Discussion

Numerical results are presented in this section for a semi-infinite medium with thermomechanical properties (Table 1) typical of carbon (Gong and Komvopoulos, 2004). Analytical solutions for a single asperity sliding over the semi-infinite are presented first to validate the algorithm and in order to establish a reference for comparison with the results obtained for a sliding rough surface, illustrating the effects of surface topography and interaction between neighboring asperities on the temperature and stress fields in the elastic medium.

4.1 Single Asperity Sliding

Numerical results for a rigid cylindrical asperity are contrasted with theoretical results in order to demonstrate the accuracy of the algorithm derived from the presented analysis. Figure 3(a) shows the deformed surface of the elastic medium due to different loading conditions for $d_{\max}/R$ = 0.0075, where $d_{\max}$ is the maximum surface interference and R is the asperity radius.

The x and z coordinates were normalized by the half-contact width corresponding to pure indentation, r_i. Normal contact produces a symmetric deformation surface profile, while normal and tangential traction (m = 0.5) produce pile-up and sink-in at the rear and front of the contact region, respectively. Thermoelastic deformation enhances pile-up at the rear of the contact region due to frictional heating (Pe = 0.05). The good match between the deformed surface and the asperity profile within the contact region illustrates the accuracy of the thermomechanical contact algorithm. Figure 3(b) shows the contact pressure distribution for $d_{\max}/R$ = 0.0075. The contact pressure was normalized by the maximum contact pressure obtained under pure indentation, p_{oi}. The curves represent numerical results and the symbols theoretical results (Johnson, 1985). The contact pressure profile is not symmetric in the presence of shear traction. The peak contact pressure predicted by the theoretical solution and the present analysis occurs at x_0/r_i = 0.092 and 0.088, respectively. The good agreement between numerical and theoretical results for the contact pressure distribution indicates the accuracy of the piecewise-linear distribution of the contact pressure profile, obtained by the superposition of overlapping triangular pressure elements. For fixed surface interference, frictional heating induces larger contact area and higher contact pressure. This is expected because frictional heating causes thermal expansion due to the development of temperature gradients, which increases both the contact area and the contact pressure.

The variation of the surface temperature distribution with the Peclet number is shown in Fig. 4 for m = 0.5 and $d_{\max}/R$ = 0.0075. In this figure, as well as in subsequent figures, the results are presented as a temperature rise from the room temperature, ΔT, normalized by $2q_a\kappa/\pi kv$, where q_a is the average heat flux rate at the contact region (i.e., total heat flux divided by the contact area), and the x coordinate is normalized by the half-contact width, r. The surface temperature

increases significantly with the increase of the Peclet number. For Pe < 0.5, the surface temperature distribution is symmetric, while for Pe > 0.5 the maximum surface temperature shifts from the center toward the trailing edge of the contact region, in agreement with the result of Carslaw and Jaeger (1959) for a moving heat source and the three-dimensional numerical result of Gong and Komvopoulos (2004) for a spherical indenter sliding on a half-space medium. Following an approach similar to that for a uniform heat band source (Carslaw and Jaeger, 1959), the temperature rise due to a moving heat band that is elliptically distributed over region $-b \le x \le b$ was obtained as

$$\Delta T = \frac{q_0^T b}{pk} \int_{-1}^{1} \sqrt{1-h^2}\, e^{-Pe(x+h)} K_0\{Pe[(x+h)^2 + z^2]^{1/2}\} dh \,. \tag{24}$$

Figure 4 shows that the normalized maximum temperature rise for Pe = 10 is equal to 2.59, which differs only by 0.4% from the theoretical solution obtained from Eq. (24). This confirms the accuracy of the present algorithm. To examine the dependence of the subsurface temperature field on the Peclet number, temperature contours for Pe = 0.05 and 5, m = 0.5, and $d_{\max}/R$ = 0.0075 are contrasted in Fig. 5. For relatively low Peclet number (Pe = 0.05), the temperature field is almost symmetric with respect to the contact region (Fig. 5(a)). However, for relatively high Peclet number (Pe = 5), the temperature field is greatly distorted and the maximum temperature occurs at the trailing edge of the contact region (Fig. 5(b)). In addition, the temperature field is significantly intensified with the increase of the Peclet number.

The effect of frictional heating on the surface stress s_{xx} is illustrated in Fig. 6 for m = 0.5 and $d_{\max}/R$ = 0.0075. The surface stress s_{xx} was normalized by the maximum contact pressure, p_0, and the x coordinate by the half-contact width for the elastic case, r_0. Frictional heating produces a profound decrease of the surface tensile stress at the trailing edge of the contact region (Pe = 49). Such high Peclet number produces a compressive s_{xx} stress in the wake of the contact

region, while in the absence of frictional heating the stress is tensile (elastic case). Therefore, surface cracking is less likely to occur under conditions promoting significant frictional heating.

Figure 7 shows the effect of frictional heating on the subsurface von Mises equivalent stress, s_M, for m = 0.5 and $d_{\max}/R$ = 0.0075. (The same contour levels are used for comparison purposes.) The Mises stress was normalized by the maximum contact pressure, p_0, and the x and z coordinates by the half-contact width obtained for the elastic case, r_0. Frictional heating (Pe = 49) intensifies the subsurface stress field. This is because the compressive stress field due to frictional heating enhances significantly the subsurface stresses below the contact region. The results shown in Fig. 7 are consistent with the finite element results of Ye and Komvopoulos (2003) that show an increase in the Mises stress due to frictional heating. The maximum value of s_M/p_0 in the thermoelastic case is equal to 1.42, which is 48% higher than that in the elastic case. The dimensionless maximum surface tensile stress, $s_{xx}^{\max}/p_0$, and von Mises equivalent stress, $s_M^{\max}/p_0$, are plotted as a function of Peclet number in Fig. 8 for m = 0.5 and $d_{\max}/R$ = 0.0075. The surface $s_{xx}^{\max}$ stress decreases and the $s_M^{\max}$ stress increases with the increase of the Peclet number due to the significant compressive stress induced by frictional heating. Hence, surface plasticity is more likely to occur than surface cracking under sliding conditions involving a high Peclet number.

4.2 Rough Surface Sliding

Unless otherwise stated, the numerical results for the case of rough surface sliding presented in this section are for $d_{\max}$ = 1.5 nm, L = 5 μm, D = 1.44, and G = 9.46 × 10^{-4} nm. For generality, results for the temperature rise are shown in dimensionless form, $\Delta T/(2q_a k/\pi kV)$.

Figure 9 shows the surface deformation of the elastic half-space due to sliding of a rough surface from left to right due to different types of loading. Figure 9(a) shows the establishment of four asperity microcontacts at the contact region. The high magnification of a segment of the surface profile shown in Fig. 9(b) demonstrates that the deformed surface follows very closely the contour of the rough surface. The exact match between the deformed surface of the half-space and the rough surface illustrates the accuracy of the algorithm. For pure normal indentation (m = 0) the total contact width is 23.6 nm, increasing to 28.8 nm with the occurrence of frictional heating (m = 0.5 and Pe = 0.06). This is a consequence of the surface pile-up induced by frictional heating that increases the real contact area, especially at the trailing contact region where thermoelastic distortion is more pronounced.

To illustrate the significance of frictional heating on the pressure distributions at asperity microcontacts, contact pressure results are shown in Fig. 10 for m = 0.5 and Pe = 54. The four plots in Fig. 10 show the contact pressure distributions in the four contact segments shown in Fig. 9. The solid curves represent numerical results for the thermoelastic case and the discontinuous curves results for elastic sliding contact. The contact pressures and the microcontact areas in the thermoelastic case are larger than those in the elastic case. This is mostly pronounced at the fourth asperity microcontact (segment 4) due to the greater cumulative effect of frictional heating at the trailing contact region.

Figure 11 shows the effect of the Peclet number of the distribution of the dimensionless surface temperature rise due to sliding (m = 0.5). For convenience, the corresponding segments of the rigid rough surface are also shown at the top of Fig. 11. For low Peclet number (Pe = 0.06) the temperature at the front of the contact region is quite close to that encountered at the wake of sliding, i.e., the temperature distribution is almost symmetric within each microcontact region

(Fig. 11(a)). However, in the case of relatively high Peclet number (Pe = 6), the temperature rise at the wake of sliding is significantly higher than that at the contact front (Fig. 11(b)), consistent with the results obtained for the single-asperity case (Fig. 4). In addition, the surface temperature for Pe = 6 is much higher than that for Pe = 0.06, evidently due to the more pronounced effect of frictional heating. For both low and high Peclet numbers, the maximum temperature rise at the surface occurs at the second microcontact (segment 2) due to the correspondingly much larger contact area (Fig. 10). Conversely to the first and second microcontacts (segments 1 and 2, respectively), the temperature at the front of the third and fourth microcontacts (segments 3 and 4, respectively) does not decrease to zero due to the more pronounce cumulative thermal effect at the trailing contact region.

Contours of normalized temperature rise, $\Delta T/(2q_a k/pkV)$, in the subsurface of the semi-infinite medium for Pe = 0.06 and 6, corresponding to the segments shown in Figs. 10 and 11, are contrasted in Fig. 12. It is noted that, for both low and high Peclet numbers, the maximum temperature rise at each microcontact always occurs at the surface. As expected, the temperature rises for Pe = 6 are much higher than those for Pe = 0.06. The appreciably higher temperature gradients produced with the higher Peclet number are responsible for the increase of the thermoelastic surface distortion and the intensification of the thermal stress. Comparison of Figs. 12(a) and 12(b) shows a profound effect of the Peclet number on the subsurface temperature distribution. The temperature contours for Pe = 6 are significantly distorted compared to those for Pe = 0.06, which are fairly symmetric.

The significance of the surface topography on the temperature rise can be interpreted in light of the dimensionless maximum temperature rise, $DT_{\max}/(2q_a k/pkV)$, shown as a function of Pe and D in Fig. 13. The maximum temperature rise increases monotonically with the Peclet

number due to the increase of the frictional heat at the sliding interface. For given Peclet number and maximum surface interference, the maximum temperature rise increases with the decrease of the fractal dimension. This is due to the dependence of the dominant frequencies in the surface profile on the value of *D*. Smaller *D* values are associated with rougher surfaces yielding asperity microcontacts of smaller radius of curvature that produce higher mean contact pressures and smaller contact areas. For fixed Peclet number, smaller contact areas imply higher sliding speed. Thus, the combination of higher contact pressure and sliding speed, obtained with small D values, enhances frictional heating, which, in turn, leads to an increase in the temperature rise at the surface.

Figure 14 shows the effect of frictional heating on the stress, s_{xx}, at the surface of the semi-infinite medium. Four asperity microcontacts are established at the contact interface, as shown in Fig. 9. The solid curves denote numerical results from the thermoelastic analysis for Pe = 54, while the discontinuous curves represent results from the elastic analysis of sliding contact. Frictional heating decreases the tensile stress at the trailing edge of each microcontact region and shifts the location of the maximum tensile stress slightly toward the trailing contact edge. Again, the largest differences between thermomechanical and mechanical results are encountered in the segment of the profile corresponding to the largest microcontact area (segment 2).

Figure 15 shows contours of von Mises equivalent stress in the subsurface corresponding to the segments shown in Fig. 14. For clarity and comparison purposes, different contour levels are used for each microcontact stress field. Comparison of Figs. 15(a) and 15(b) shows that frictional heating increases the Mises stress, especially below the third and fourth microcontacts (segments 3 and 4, respectively) due to the greater cumulative effect of frictional heating. The maximum von Mises stress in the thermomechanical case is equal to 7.01 GPa (Fig. 15(b)), which is 23%

higher than that obtained in the elastic analysis (Fig. 15(a)). The results shown in Fig. 15 are consistent with finite element simulation results of Ye and Komvopoulos (2003) demonstrating that the maximum Mises stress at each microcontact always occurs at the surface when the coefficient of friction is relatively high (e.g., m = 0.5) and that frictional heating affects the location of the maximum Mises stress, as seen for the second microcontact in Fig. 15.

The maximum tensile stress at the surface, $s_{xx}^{\max}$, and maximum von Mises equivalent stress in the subsurface, $s_M^{\max}$, versus Peclet number are compared in Fig. 16. The $s_{xx}^{\max}$ stress increases slightly with the increase of the Peclet number in the range of Pe < 20 due to the dominant effect of the increasing mean contact pressure. However, when Pe > 20, $s_{xx}^{\max}$ decreases due to the dominant effect of the increasing compressive thermal stress, which is enhanced by the interaction of neighboring microcontacts. The fact that $s_M^{\max}$ increases when Pe > 20 suggests that the contribution of thermal stresses is comparable with that of the mechanical stresses. The small variations of $s_{xx}^{\max}$ and $s_M^{\max}$ when Pe < 20 suggests that, at relatively low and intermediate values of the Peclet number, the stress field is dominated by the mechanical stresses and so the effect of thermal stresses due to frictional heating is secondary.

5. Conclusions

A thermomechanical analysis of sliding contact was presented for elastic semi-infinite solids with surface topographies characterized by fractal geometry. The effect of frictional heating on the contact pressure, temperature rise, and stress field was examined in terms of the Peclet number for the cases of a single asperity and a rough surface sliding over the elastic medium. Based on the presented results and discussion, the following main conclusions can be drawn.

(1) Frictional heating increases the contact area and contact pressure. This effect is mostly pronounced at asperity microcontacts located at the trailing edge of the contact interface where the cumulative effect of frictional heating is most pronounced.

(2) The surface temperature distribution at a single asperity contact is fairly symmetric for low Peclet numbers (e.g., Pe < 1). However, the peak temperature shifts toward the trailing edge of the contact region for relatively high Peclet numbers (e.g., Pe > 2.5).

(3) The maximum temperature at each microcontact always occurs at the surface and increases with the Peclet number. The intensification of the temperature gradients with the increase of the Peclet number is responsible for the increase of the thermoelastic distortion at the surface and the development of high thermal stresses. The increase of the Peclet number changes significantly the fairly symmetric subsurface temperature field at each microcontact obtained at low Peclet numbers (e.g., Pe = 0.06). The maximum temperature rise at the surface increases with the decrease of the fractal dimension.

(4) At low Peclet numbers (Pe < 1) the stress field is dominated by mechanical stresses. Frictional heating decreases the maximum tensile stresses at the trailing edges of asperity microcontacts and slightly shifts their locations toward the trailing contact edge.

(5) The von Mises equivalent stress is strongly affected by frictional heating, especially at microcontact regions close to the trailing contact edge where the highest thermal stresses are produced due to the cumulative heating effect. High friction (m = 0.5) increases the maximum Mises stress at each microcontact and shifts its location at the surface. The increase of the Peclet number promotes surface plastic deformation and reduces the probability for surface cracking.

Acknowledgments

This work was partially supported by the National Science Foundation through a subcontract from Carnegie Mellon University, and the Computer Mechanics Laboratory at the University of California at Berkeley.

References

Bailey, D. M., and Sayles, R. S., 1991, "Effect of Roughness and Sliding Friction on Contact Stresses," ASME J. Tribol., **113**, pp. 729-738.

Barber, J. R., 1984, "Thermoelastic Displacements and Stresses Due to a Heat Source Moving Over the Surface of a Half Plane," ASME J. Appl. Mech., **51**, pp. 636-640.

Berry, M. V., and Lewis, Z. V., 1980, "On the Weierstrass-Mandelbrot Fractal Function," Proc. R. Soc. (London) Series A, **370**, pp. 459-484.

Blok, H., 1937, "Theoretical Study of Temperature Rise at Surfaces of Actual Contact Under Oiliness Lubricating Conditions," Proceedings General Discussion on Lubrication and Lubricants, Institute of Mechanical Engineers (London), **2,** pp. 222-235.

Carslaw, H. S., and Jaeger, J. C., 1959, *Conduction of Heat in Solids*, Clarendon Press, Oxford.

Cho, S.-S., and Komvopoulos, K., 1997, "Thermoelastic Finite Element Analysis of Subsurface Cracking Due to Sliding Surface Traction," ASME J. Eng. Mater. Technol., **119**, pp.71-78.

Gong, Z.-Q., and Komvopoulos, K., 2004, "Mechanical and Thermomechanical Elastic-Plastic Contact Analysis of Layered Media with Patterned Surfaces," ASME J. Tribol., **126**, pp. 9-17.

Gupta, V., Bastias, P., Hahn, G. T., and Rubin, C. A., 1993, "Elastoplastic Finite-Element Analysis of 2-D Rolling-Plus-Sliding Contact With Temperature-Dependent Bearing Steel Material Properties," Wear, **169**, pp.251–256.

Huang, J. H., and Ju, F. D., 1985, "Thermomechanical Cracking Due to Moving Frictional Loads," Wear, **102**, pp. 81-104.

Jaeger, J. C., 1942, "Moving Sources of Heat and the Temperature at Sliding Contacts," Proceedings Royal Society of NS Wales, **76**, pp. 203-224.

Johnson, K. L., 1985, *Contact Mechanic*s, Cambridge University Press, Cambridge, UK.

Ju, Y., and Farris, T. N., 1997, "FFT Thermoelastic Solutions for Moving Heat Sources," ASME J. Tribol., **119**, pp. 156-162.

Ju, F. D., and Huang, J. H., 1982, "Heat Checking in the Contact Zone of a Bearing Seal (A Two-Dimensional Model of a Single Moving Asperity)," Wear, **79**, pp. 107-118.

Ju, F. D., and Liu, J. C., 1988, "Effect of Peclet Number in Thermo-Mechanical Cracking Due to High-Speed Friction Load," ASME J. Tribol., **110**, pp. 217-221.

Komvopoulos, K., 2000, "Head-Disk Interface Contact Mechanics for Ultrahigh Density Magnetic Recording," Wear, **238**, pp. 1-11.

Komvopoulos, K., and Yan, W., 1997, "A Fractal Analysis of Stiction in Microelectromechanical Systems," ASME J. Tribol., **119**, pp. 391-400.

Leroy, J. M., Floquet, A., and Villechaise, B., 1989, "Thermomechanical Behavior of Multilayered Media: Theory," ASME J. Tribol., **111**, pp. 538-544.

Liu, G., and Wang, Q., 2000, "Thermoelastic Asperity Contacts, Frictional Shear, and Parameter Correlations," ASME J. Tribol., **122**, pp. 300-307.

Liu, S. B., and Wang, Q., 2001, "A Three-Dimensional Thermomechanical Model of Contact Between Non-Conforming Rough Surfaces," ASME J. Tribol., **123**, pp. 17-26.

Liu, S. B., and Wang, Q., 2003, "Transient Thermoelastic Stress Fields in a Half-Space," ASME J. Tribol., **125**, pp. 33-43.

Mandelbrot, B. B., 1983, *The Fractal Geometry of Nature*, Freeman, New York.

Tian, X. F., and Kennedy, F. E., 1994, "Maximum and Average Flash Temperatures in Sliding Contacts," ASME J. Tribol., **116**, pp. 167–174.

Uetz, H., and Föhl, J., 1978, "Wear as an Energy Transformation Process," Wear, **49**, pp. 253-264.

Wang, Q., and Liu, G., 1999, "A Thermoelastic Asperity Contact Model Considering Steady-State Heat Transfer," Tribol. Trans., **42**, pp. 763–770.

Wang, S. and Komvopoulos, K., 1994, "A Fractal Theory of the Interfacial Temperature Distribution in the Slow Sliding Regime: Part I - Elastic Contact and Heat Transfer Analysis," ASME J. Tribol., **116**, pp. 812-823.

Ye, N., and Komvopoulos, K., 2003, "Three-Dimensional Finite Element Analysis of Elastic-Plastic Layered Media Under Thermomechanical Surface Loading," ASME J. Tribol., **125**, pp. 52-59.

Table 1. Thermomechanical properties of semi-infinite solid

Property	Magnitude
Elastic modulus, E (GPa)	168
Poisson's ratio, n	0.3
Thermal expansion, a (K^{-1})	3.1×10^{-6}
Specific heat, c (J/g·K)	0.5
Conductivity, k (W/m·K)	0.052, 0.52, 5.2
Density, r (kg/m^3)	2.15×10^3
Diffusivity, k (m^2/s)	$4.84 \times (10^{-8}, 10^{-7}, 10^{-6})$

List of Figures

Fig. 9 (a) Deformed surface and (b) segment of interfacial region of elastic semi-infinite solid subjected to different loadings by a rigid rough (fractal) surface (D = 1.44, G = 9.46 × 10^{-4} nm, m = 0.5, d_{max} = 1.5 nm, and Pe = 0.06).

Fig. 10 Contact pressure on elastic semi-infinite solid in normal contact with a rigid rough (fractal) surface (D = 1.44, G = 9.46 × 10^{-4} nm, m = 0.5, and d_{max} = 1.5 nm). Solid and discontinuous curves represent thermoelastic (Pe = 54) and elastic results, respectively.

Fig. 11 Dimensionless temperature rise $\Delta T/(2q_a k/pkV)$ at the surface of elastic semi-infinite solid in sliding contact with a rigid rough (fractal) surface (D = 1.44, G = 9.46 × 10^{-4} nm, m = 0.5, and d_{max} = 1.5 nm): (a) Pe = 0.06 and (b) Pe = 6.

Fig. 12 Contours of dimensionless temperature rise $\Delta T/(2q_a k/pkV)$ in the subsurface of elastic semi-infinite solid in sliding contact with a rigid rough (fractal) surface (D = 1.44, G = 9.46 × 10^{-4} nm, m = 0.5, and d_{max} = 1.5 nm): (a) Pe = 0.06 and (b) Pe = 6.

Fig. 13 Dimensionless maximum temperature rise $\Delta T_{max}/(2q_a k/pkV)$ at the surface of elastic semi-infinite solid in sliding contact with a rigid rough (fractal) surface versus Peclet number and fractal dimension (G = 9.46 × 10^{-4} nm, m = 0.5, and d_{max} = 1.5 nm).

Fig. 14 Stress s_{xx} at the surface of elastic semi-infinite solid in sliding contact with a rigid rough (fractal) surface (D = 1.44, G = 9.46 × 10^{-4} nm, m = 0.5, and d_{max} = 1.5 nm). Solid and discontinuous curves represent thermoelastic (Pe = 54) and elastic results, respectively.

Fig. 15 Contours of von Mises equivalent stress, s_M, in the subsurface of elastic semi-infinite solid in sliding contact with a rigid rough (fractal) surface (D = 1.44, G = 9.46 × 10^{-4} nm, m = 0.5, and d_{max} = 1.5 nm): (a) Pe = 0 and (b) Pe = 54.

Fig. 16 Maximum tensile stress, $s_{xx}^{\max}$, and von Mises equivalent stress, $s_{M}^{\max}$, at the surface of elastic semi-infinite solid in sliding contact with a rigid rough (fractal) surface versus Peclet number (D = 1.44, $G = 9.46 \times 10^{-4}$ nm, m = 0.5, and $d_{\max}$ = 1.5 nm).

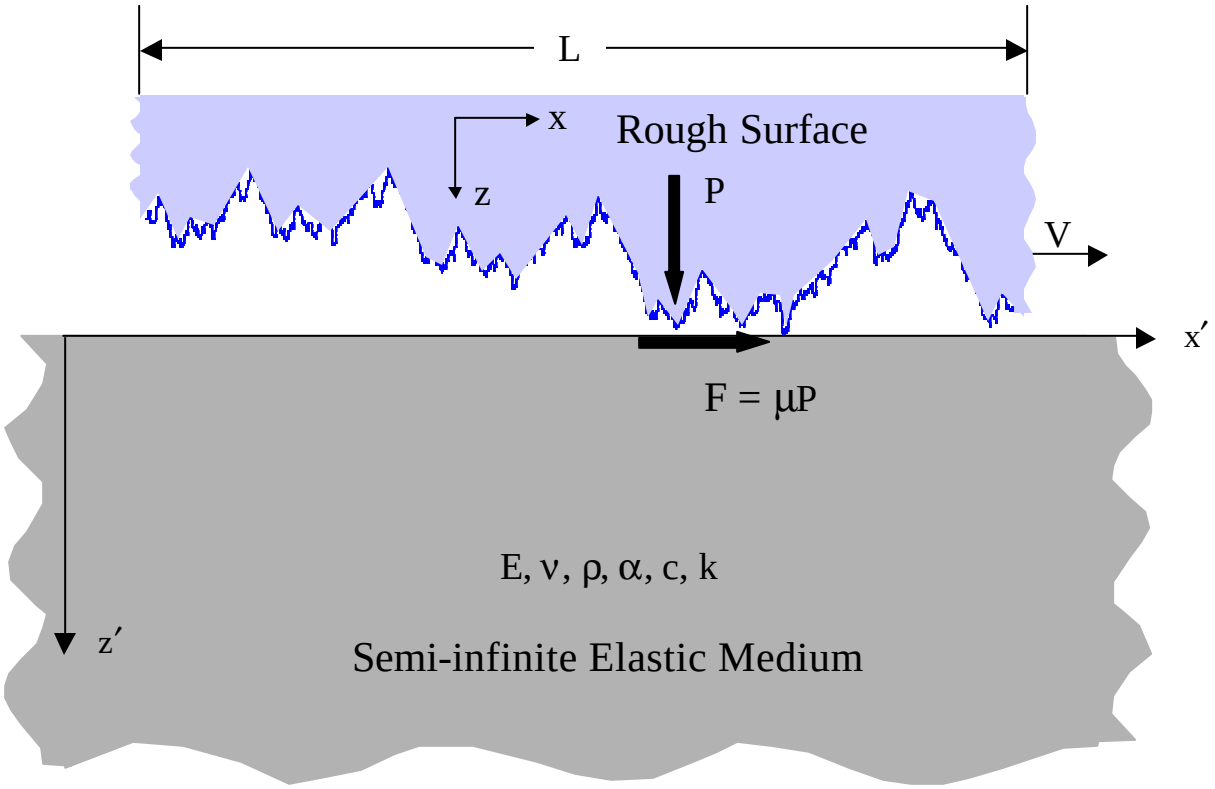
L
x
z
Rough Surface
P
V
x′
F = μP
E, ν, ρ, α, c, k
z′
Semi-infinite Elastic Medium

Figure 1

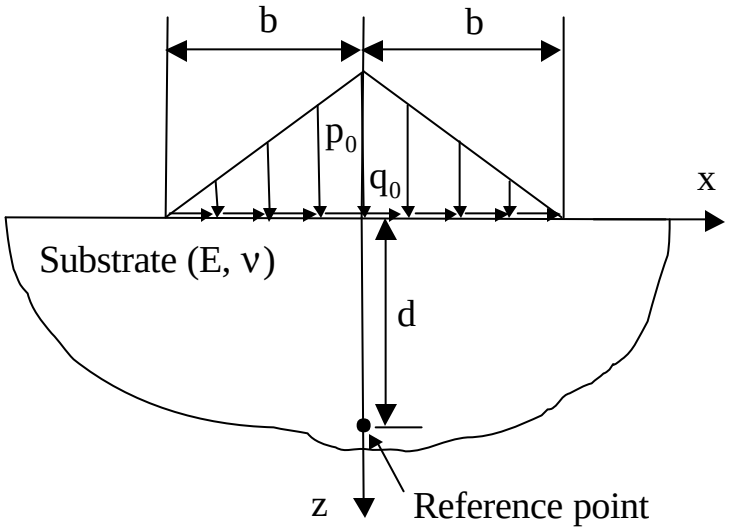
b
b
p_0
q_0
x
Substrate (E, ν)
d
z
Reference point

(a)

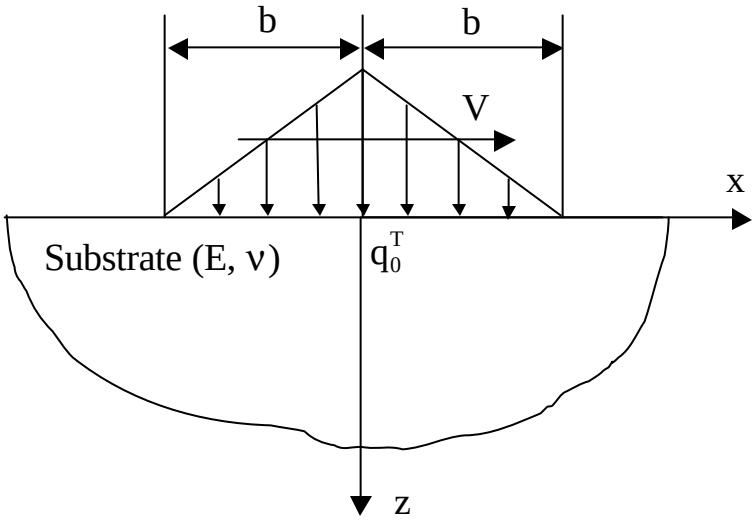
b
b
V
x
Substrate (E, ν)
q_0^T
z

(b)

Figure 2

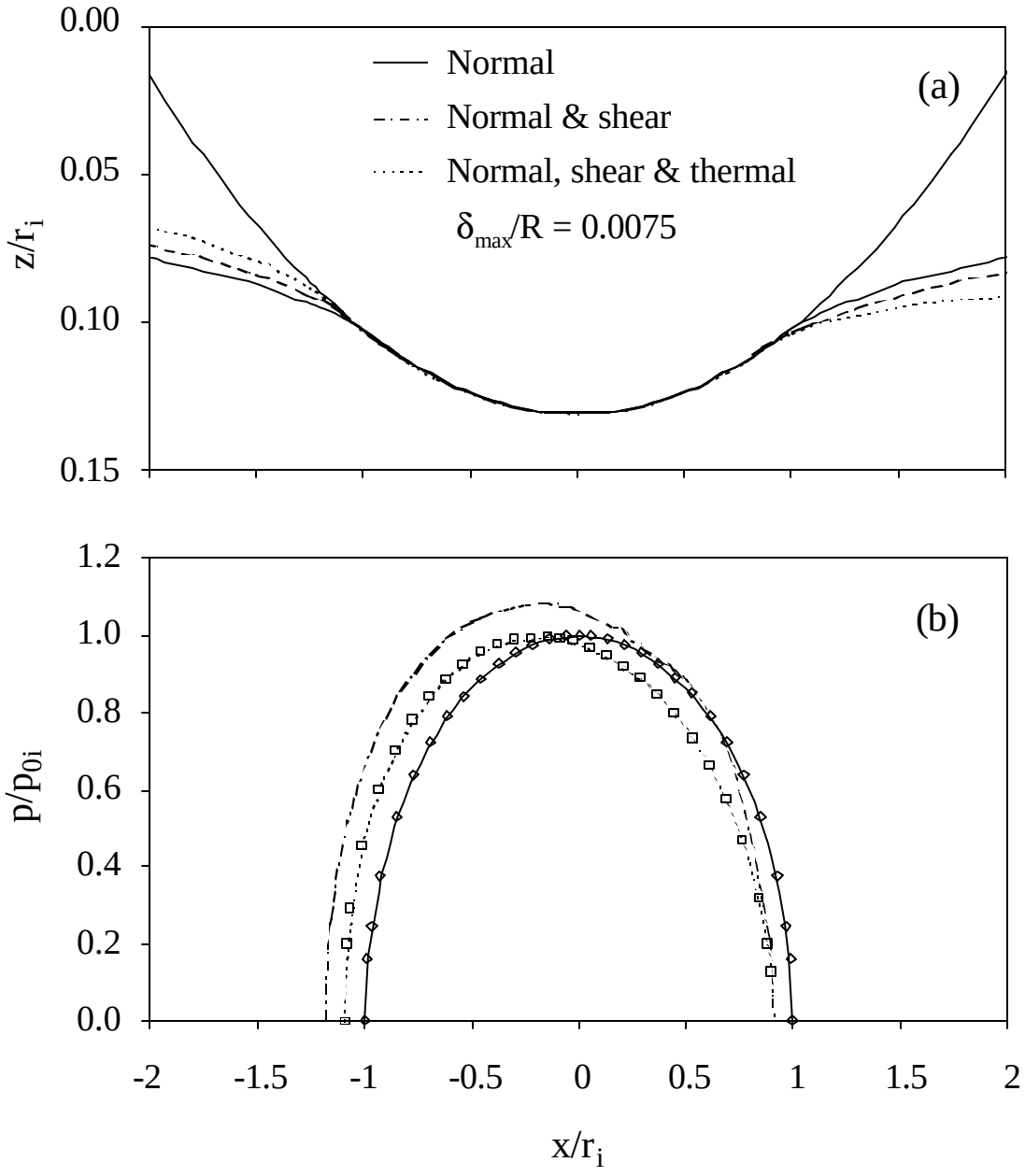
0.00
0.05
0.10
0.15
z/r_i
Normal
Normal & shear
Normal, shear & thermal
δ_max/R = 0.0075
(a)
1.2
1.0
0.8
0.6
0.4
0.2
0.0
p/p_0i
(b)
-2
-1.5
-1
-0.5
0
0.5
1
1.5
2
x/r_i

Figure 3

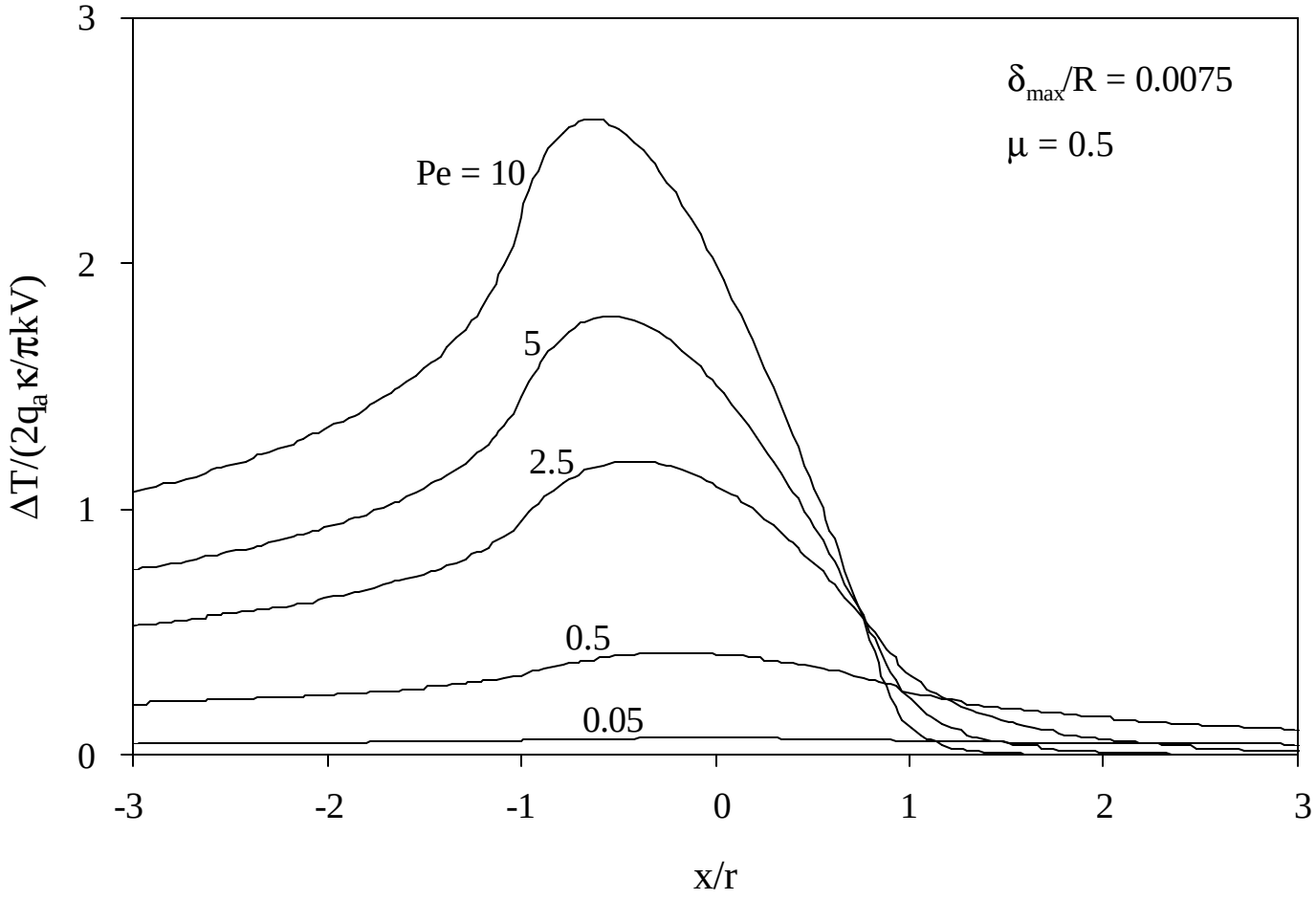
3
2
1
0
-3
-2
-1
0
1
2
3
$\delta_{max}/R = 0.0075$
$\mu = 0.5$
Pe = 10
5
2.5
0.5
0.05
$\Delta T/(2q_a \kappa/\pi kV)$
x/r

Figure 4

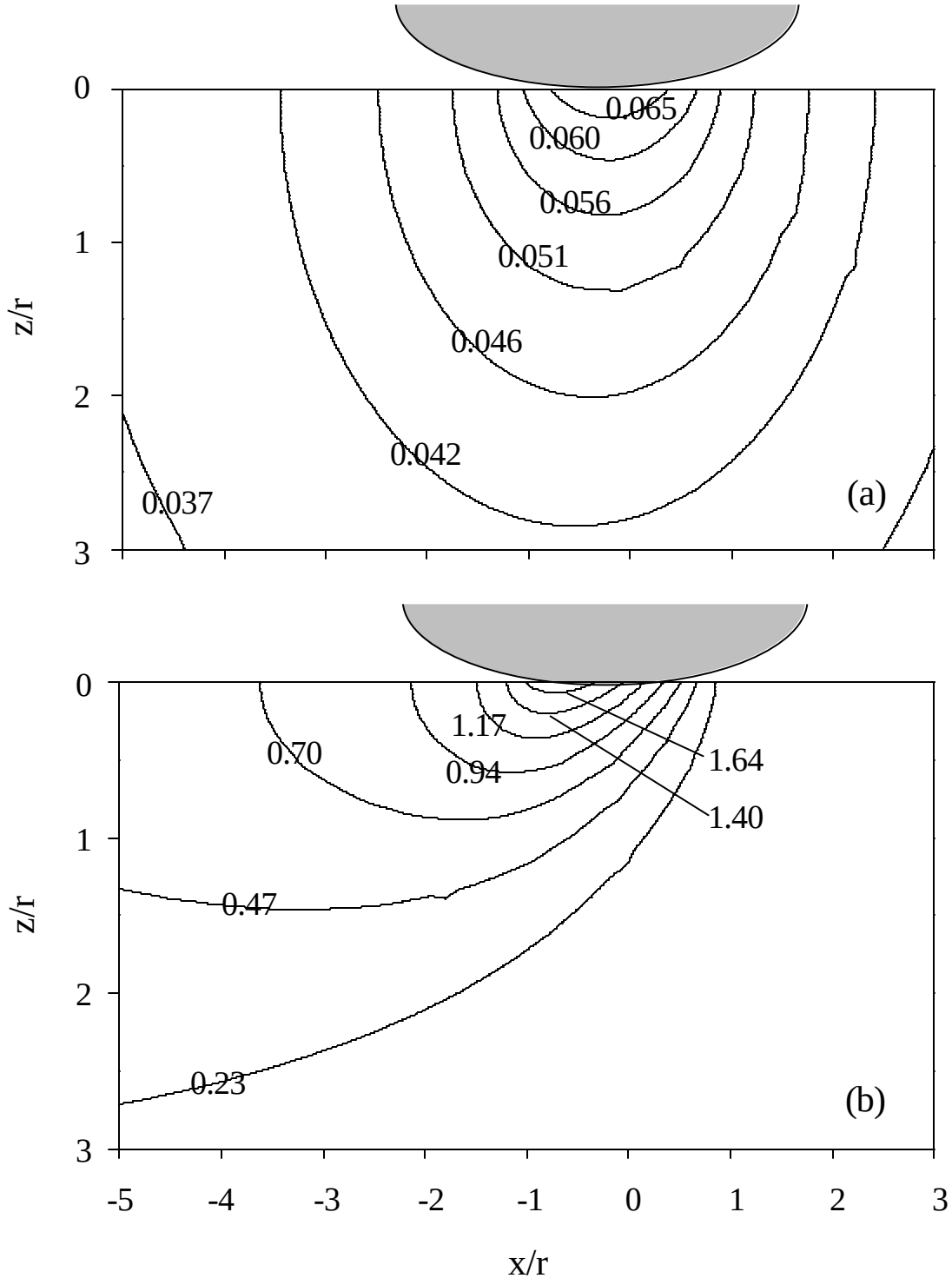
0
1
2
3
z/r
0.065
0.060
0.056
0.051
0.046
0.042
0.037
(a)
0
1
2
3
z/r
1.17
0.70
0.94
1.64
1.40
0.47
0.23
(b)
-5
-4
-3
-2
-1
0
1
2
3
x/r

Figure 5

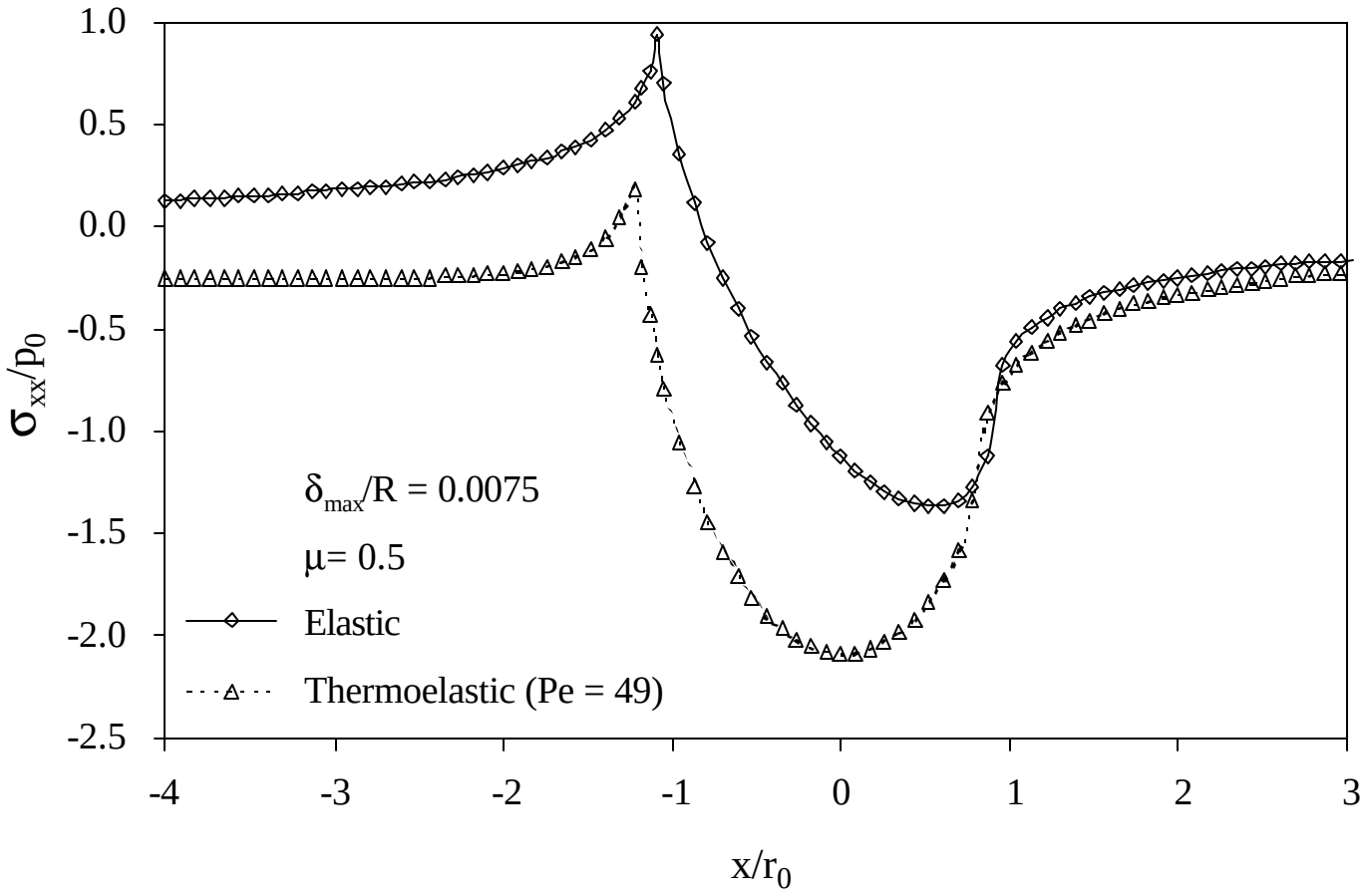
1.0
0.5
0.0
-0.5
-1.0
-1.5
-2.0
-2.5
-4
-3
-2
-1
0
1
2
3
σxx/p0
x/r0
δmax/R = 0.0075
μ= 0.5
Elastic
Thermoelastic (Pe = 49)

Figure 6

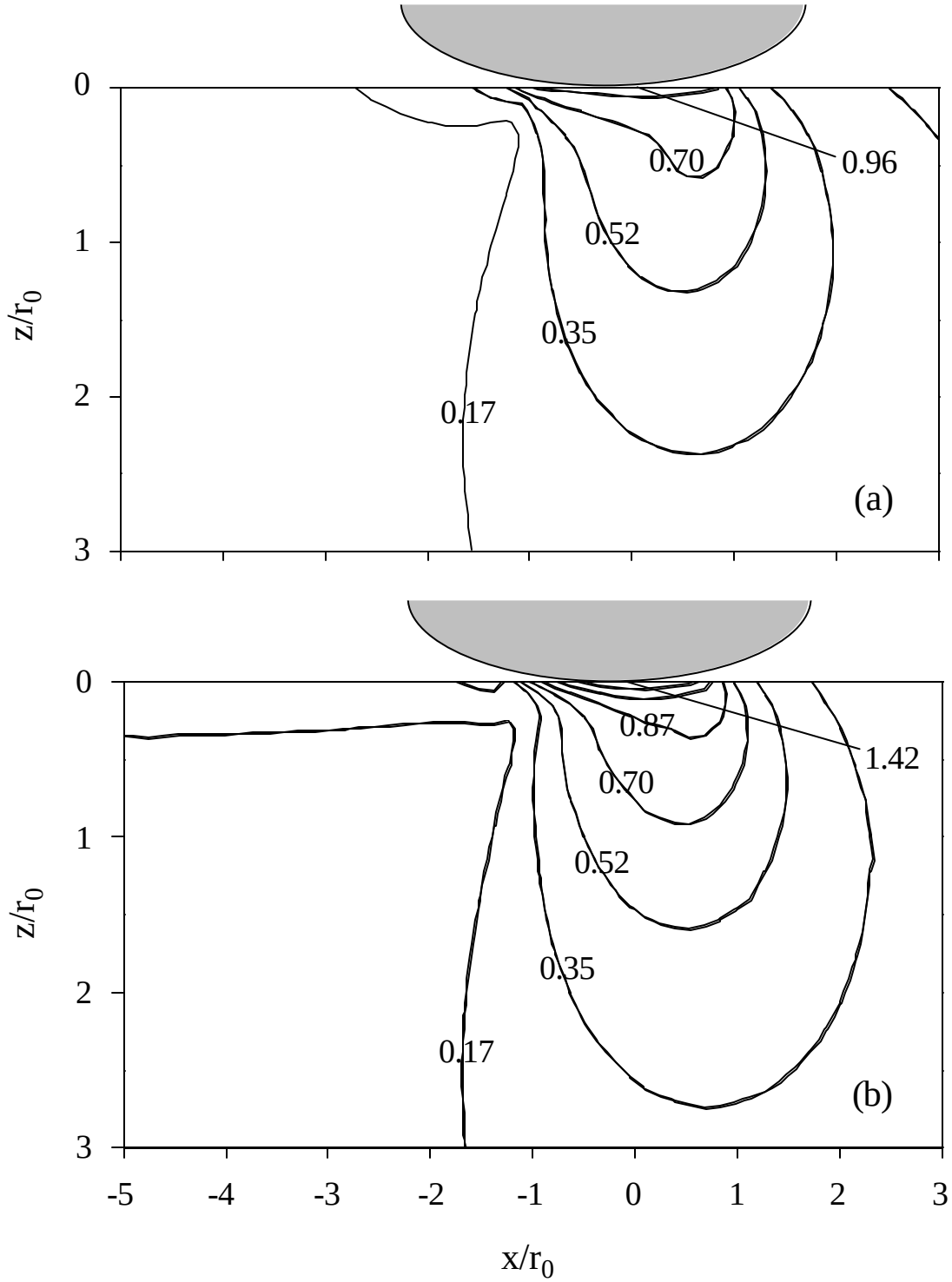
0
1
2
3
z/r0
0.70
0.96
0.52
0.35
0.17
(a)
0
1
2
3
z/r0
0.87
1.42
0.70
0.52
0.35
0.17
(b)
-5
-4
-3
-2
-1
0
1
2
3
x/r0

Figure 7

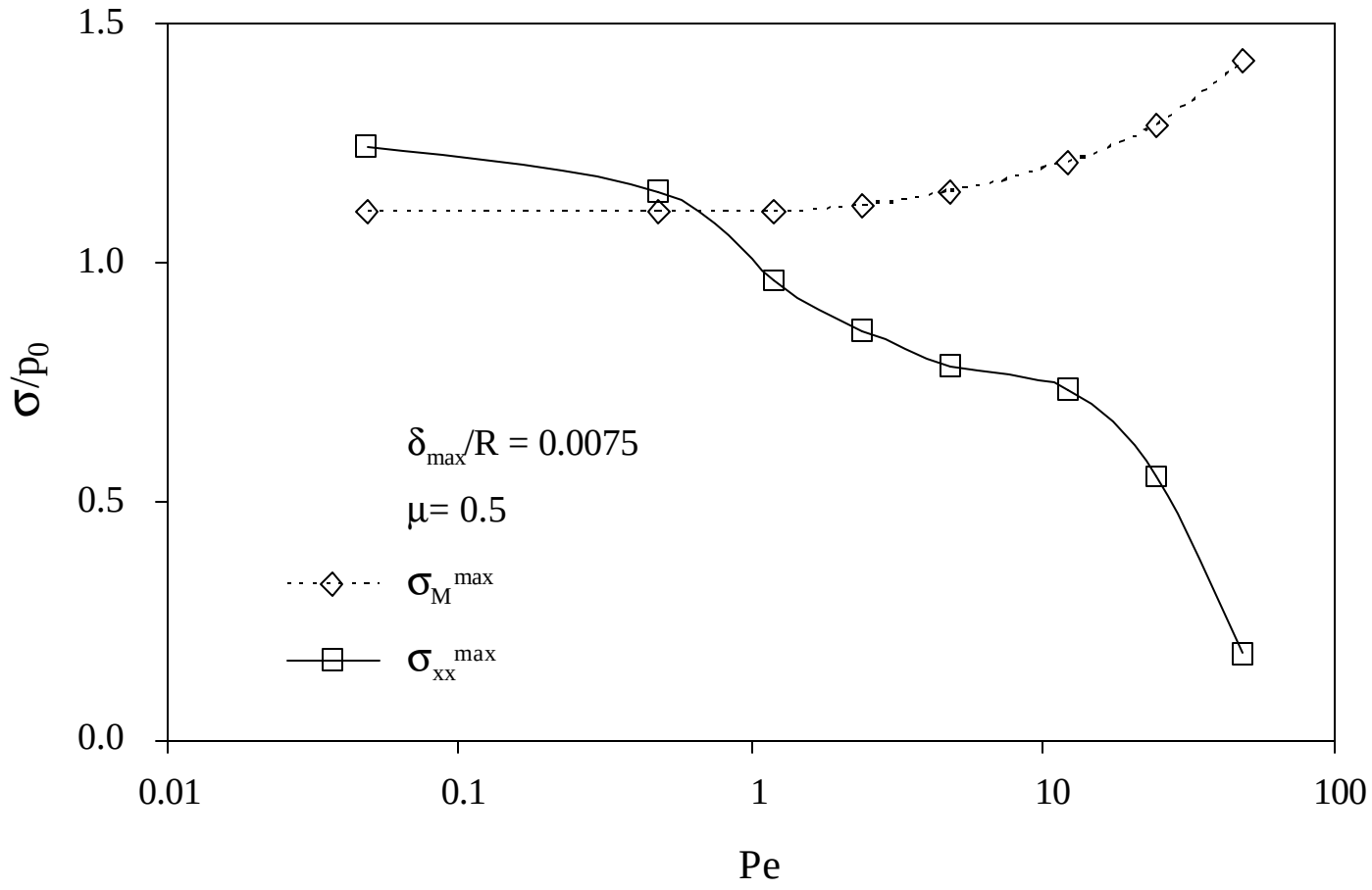

Figure 8

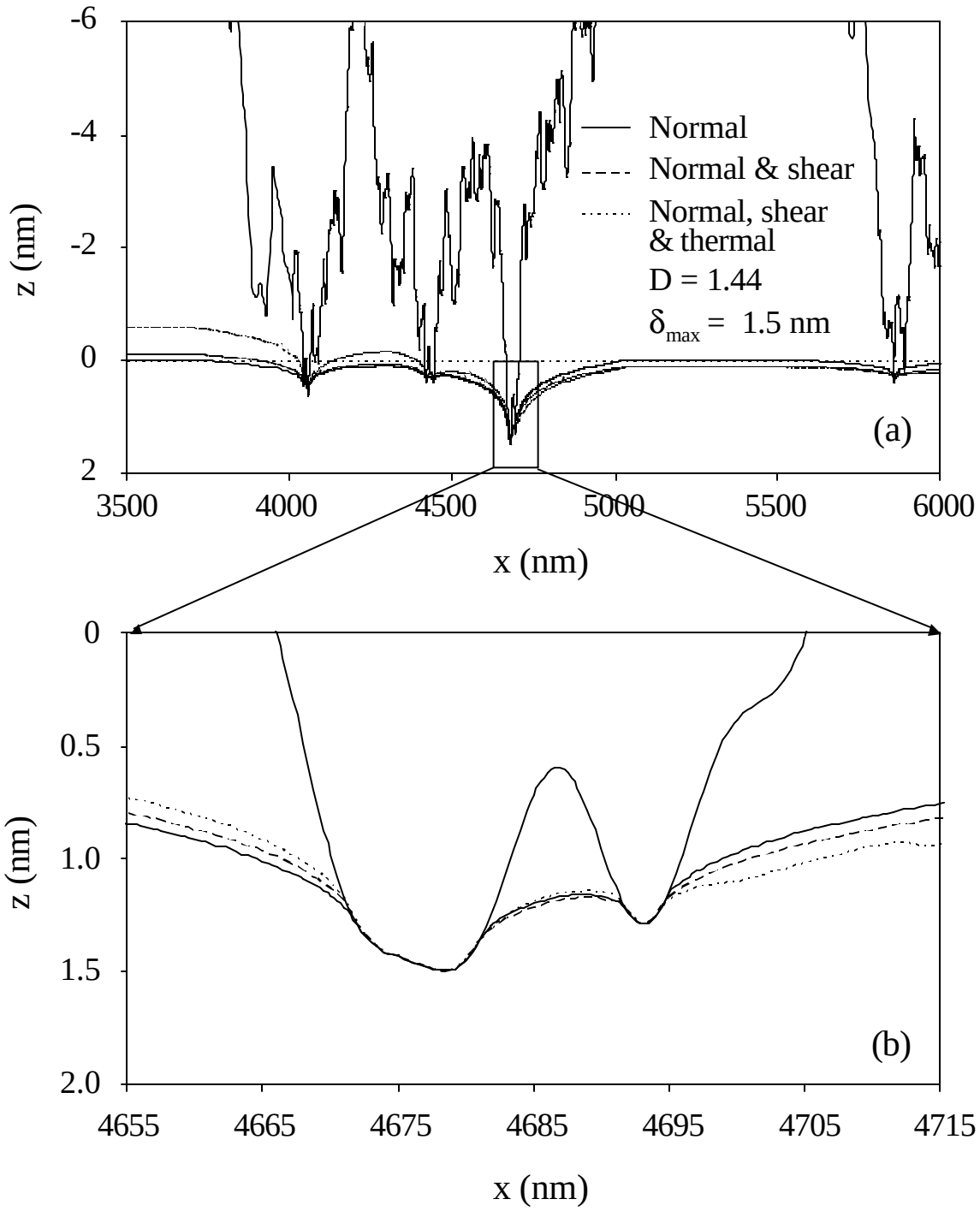
-6
-4
-2
0
2
z (nm)
Normal
Normal & shear
Normal, shear
& thermal
D = 1.44
δmax = 1.5 nm
(a)
3500
4000
4500
5000
5500
6000
x (nm)
0
0.5
1.0
1.5
2.0
z (nm)
(b)
4655
4665
4675
4685
4695
4705
4715
x (nm)

Figure 9

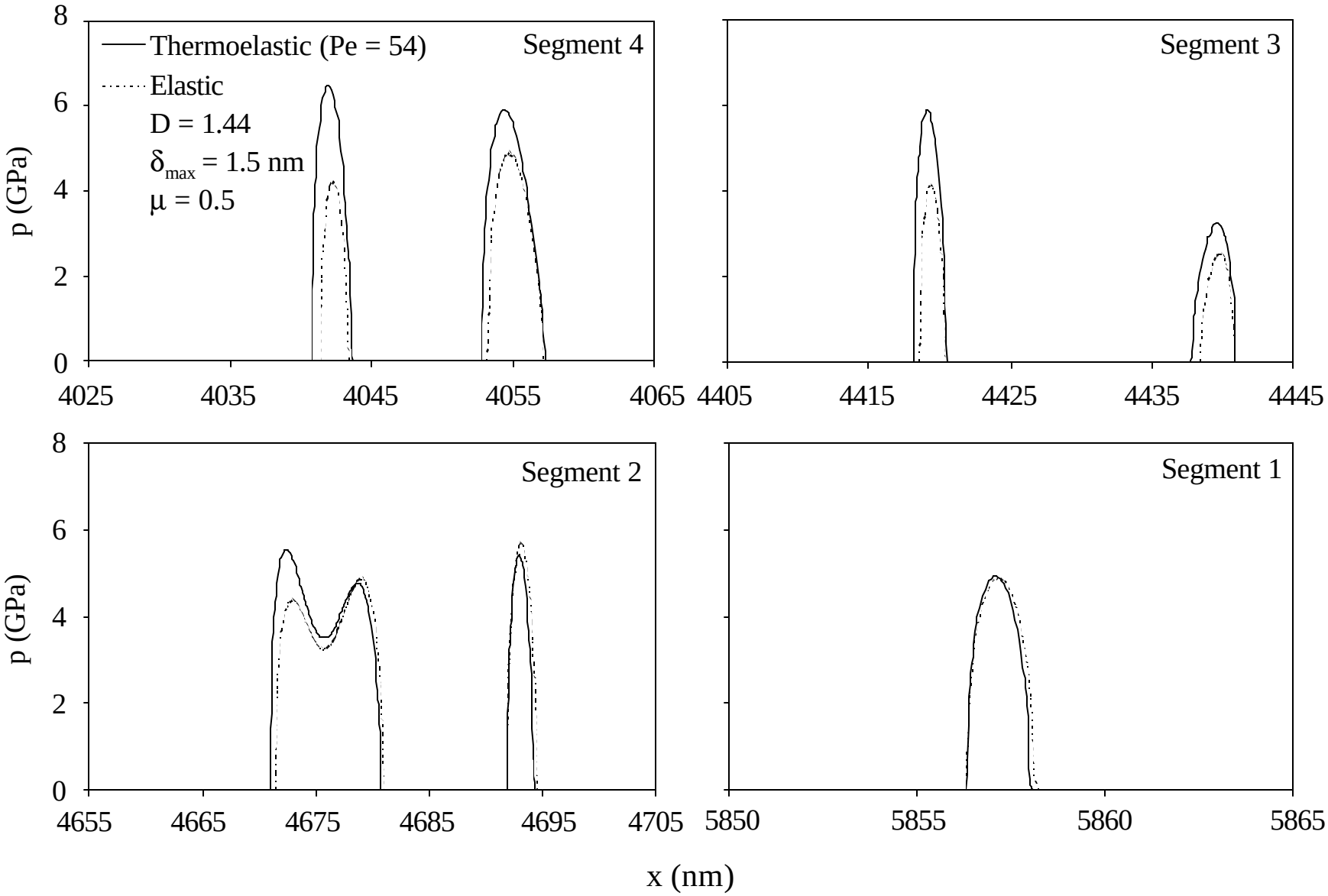
Thermoelastic (Pe = 54)
Elastic
D = 1.44
δmax = 1.5 nm
μ = 0.5
Segment 4
Segment 3
Segment 2
Segment 1
p (GPa)
x (nm)
0
2
4
6
8
4025
4035
4045
4055
4065
4405
4415
4425
4435
4445
4655
4665
4675
4685
4695
4705
5850
5855
5860
5865

Figure 10

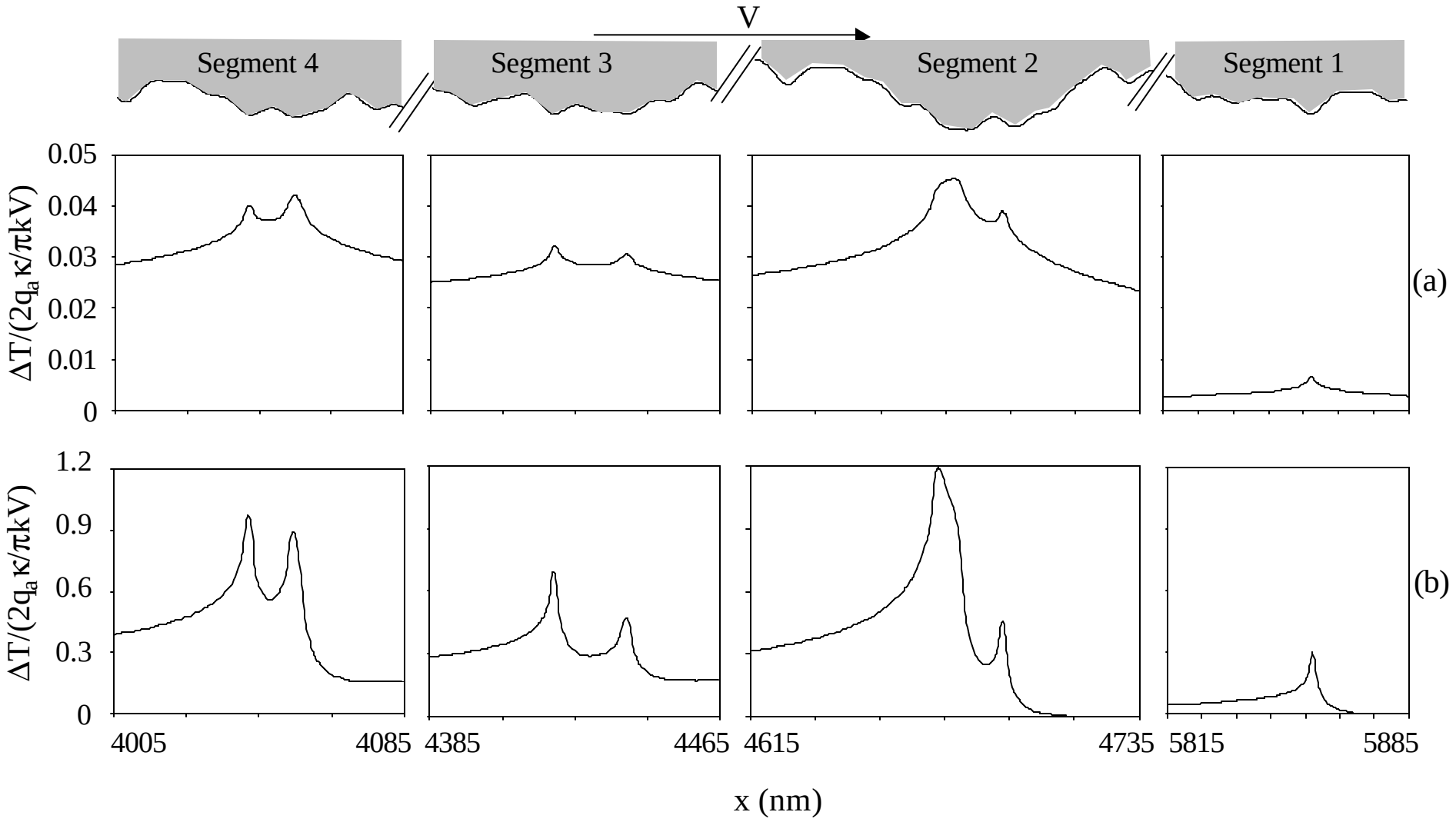
V
Segment 4
Segment 3
Segment 2
Segment 1
0.05
0.04
0.03
0.02
0.01
0
ΔT/(2q_a κ/πkV)
(a)
1.2
0.9
0.6
0.3
0
ΔT/(2q_a κ/πkV)
(b)
4005
4085
4385
4465
4615
4735
5815
5885
x (nm)

Figure 11

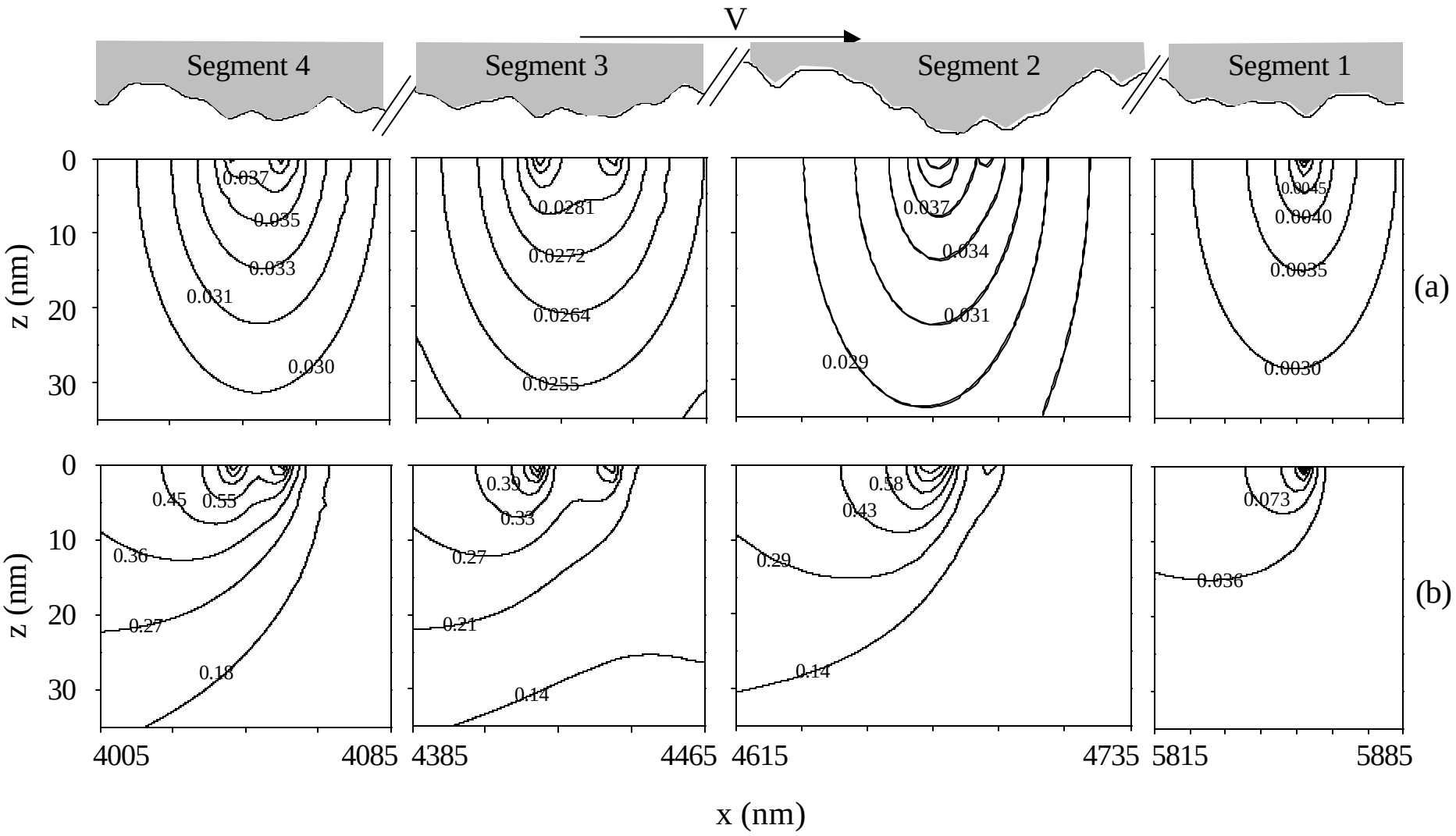
V
Segment 4
Segment 3
Segment 2
Segment 1
z (nm)
0
10
20
30
0.037
0.035
0.033
0.031
0.030
0.0281
0.0272
0.0264
0.0255
0.037
0.034
0.031
0.029
0.0045
0.0040
0.0035
0.0030
(a)
0.45
0.55
0.36
0.27
0.18
0.39
0.33
0.27
0.21
0.14
0.58
0.43
0.29
0.14
0.073
0.036
(b)
4005
4085
4385
4465
4615
4735
5815
5885
x (nm)

Figure 12

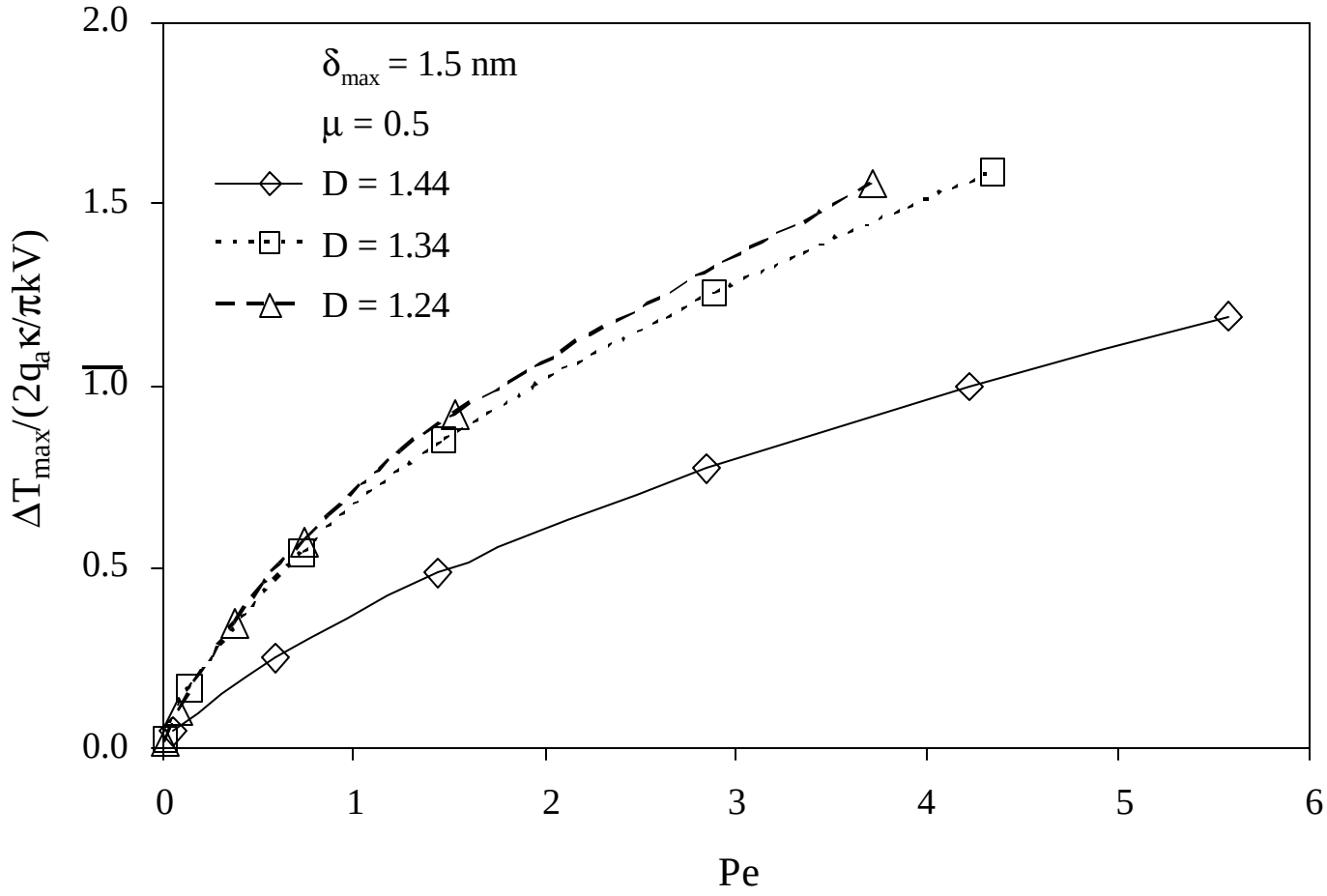
2.0
1.5
1.0
0.5
0.0
0
1
2
3
4
5
6
Pe
$\Delta T_{max}/(2q_a\kappa/\pi kV)$
δ_{max} = 1.5 nm
μ = 0.5
D = 1.44
D = 1.34
D = 1.24

Figure 13

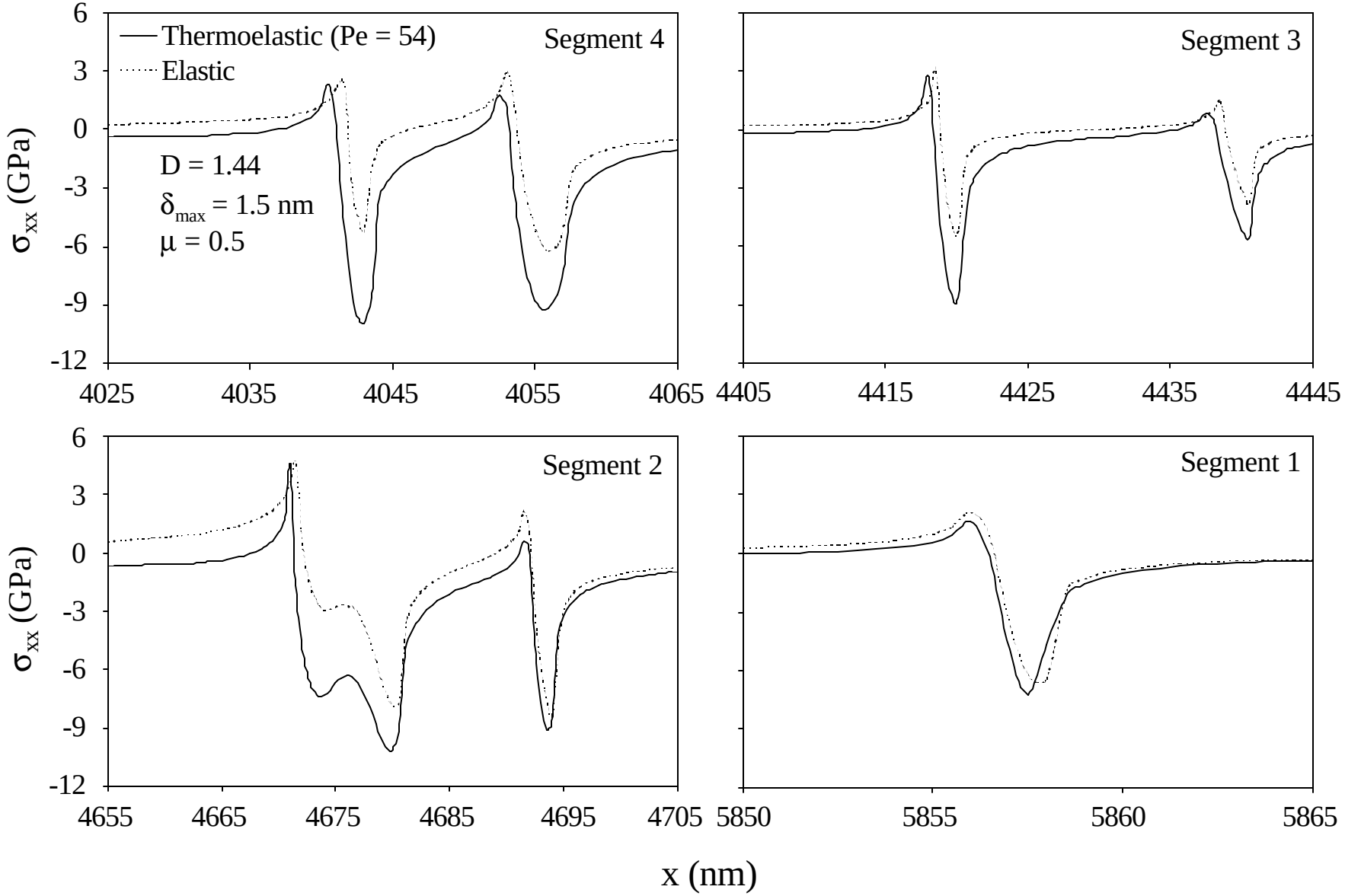
Thermoelastic (Pe = 54)
Elastic
D = 1.44
δmax = 1.5 nm
μ = 0.5
Segment 4
Segment 3
Segment 2
Segment 1
σxx (GPa)
x (nm)
6
3
0
-3
-6
-9
-12
4025
4035
4045
4055
4065
4405
4415
4425
4435
4445
4655
4665
4675
4685
4695
4705
5850
5855
5860
5865

Figure 14

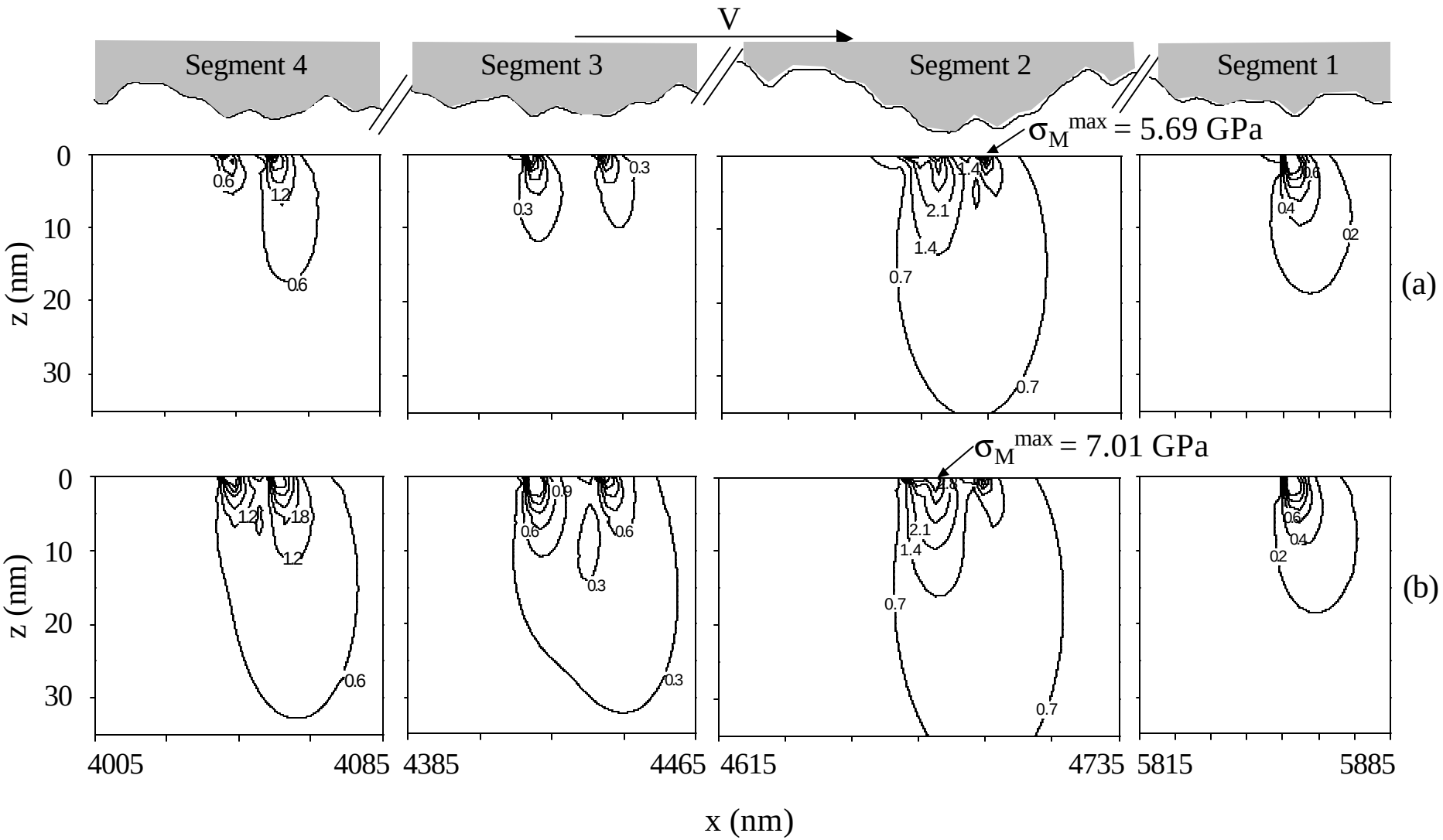
V
Segment 4
Segment 3
Segment 2
Segment 1
σM max = 5.69 GPa
σM max = 7.01 GPa
z (nm)
0
10
20
30
(a)
(b)
4005
4085
4385
4465
4615
4735
5815
5885
x (nm)

Figure 15

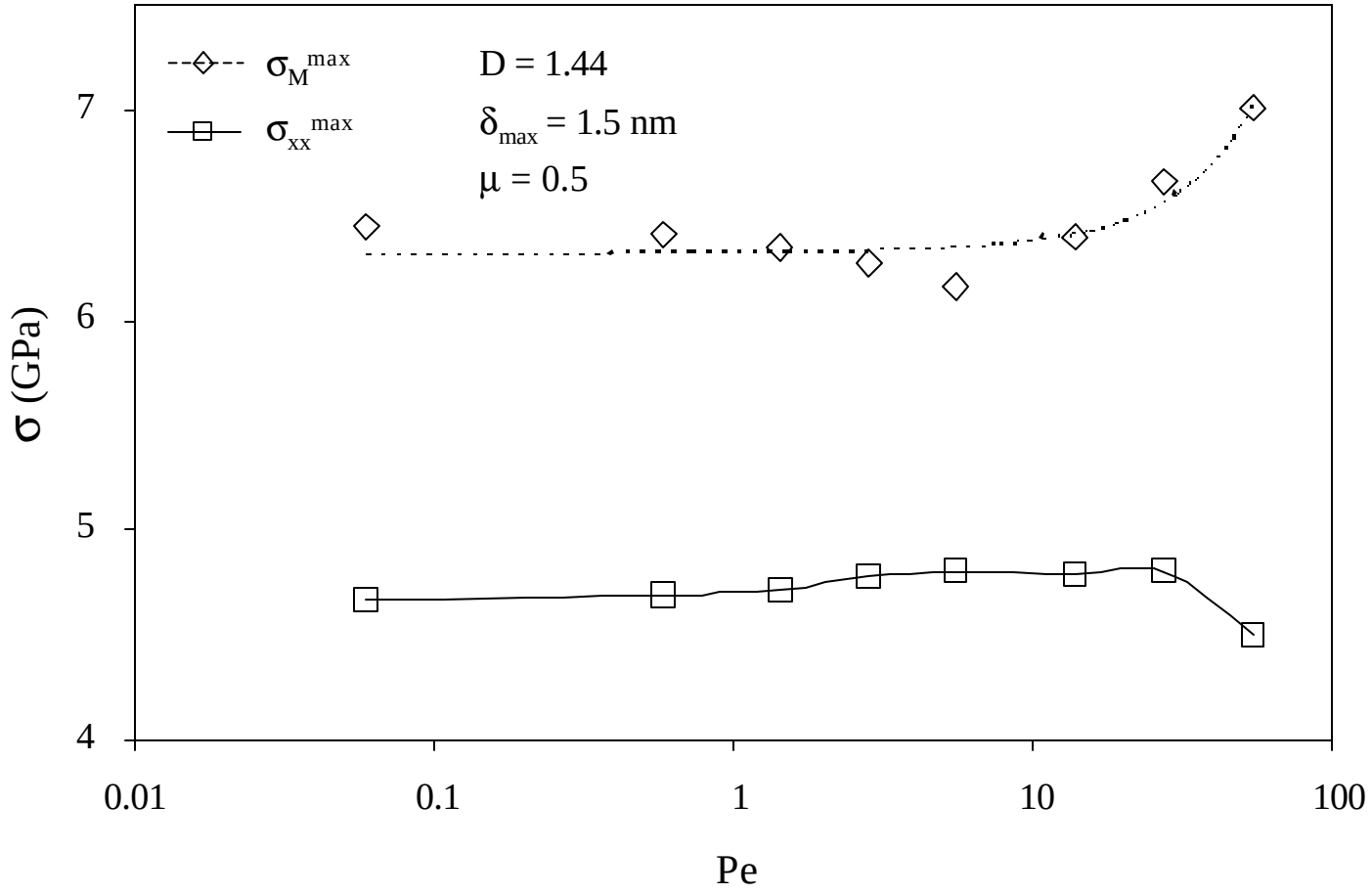

Figure 16